Compartmentalization of Axial Seamount's magma reservoir inferred by analytical and numerical deformation modeling with realistic geometry

S.R. Slead[1], M. Wei[1], S.L. Nooner[2], W.W. Chadwick[3], D.W. Caress[4], and J. Beeson[3,5]

[1]Graduate School of Oceanography, University of Rhode Island, Narragansett, RI, USA.

[2]Department of Earth and Ocean Sciences, University of North Carolina Wilmington, Wilmington, NC, USA

[3]Oregon State University, Cooperative Institute for Marine Resources Studies, Hatfield Marine Science Center, Newport, OR, USA

[4]Monterey Bay Aquarium Research Institute, Moss Landing, CA, USA

[5]National Oceanic and Atmospheric Administration, Pacific Marine Environmental Laboratory, Newport, OR, USA

Corresponding author: Sandra Slead (sslead@uri.edu)

Key Points:

- Uniform pressurization of Axial Seamount's seismically imaged magma reservoir does not adequately fit the observed geodetic data
- Our models estimate that Axial's magma reservoir inflated by 0.054-0.060 km^3 during the inter-eruptive recharge period between 2016-2020
- Axial's magma reservoir is likely compartmentalized, with magma accumulating in sills along the western-central edge of the magma reservoir

Abstract

Axial Seamount is a submarine volcano on the Juan de Fuca Ridge with enhanced magma supply from the Cobb Hotspot. Here we compare several deformation model configurations to explore how the spatial component of Axial's deformation time series relates to magma reservoir geometry imaged by multi-channel seismic (MCS) surveys. To constrain the models, we use vertical displacements from pressure sensors at seafloor benchmarks and repeat autonomous underwater vehicle (AUV) bathymetric surveys covering 2016-2020. We show that implementing the MCS-derived 3D main magma reservoir (MMR) geometry with uniform pressure in a finite element model poorly fits the geodetic data. To test the hypothesis that there is compartmentalization within the MMR that results in heterogeneous pressure distribution, we compare analytical models using various horizontal sill configurations constrained by the MMR geometry. Using distributed pressure sources significantly improved the Root Mean Square Error (RMSE) between the inflation data and the models by an order of magnitude. The RMSE between the AUV data and the models was not improved as much, likely due to the relatively larger uncertainty of the AUV data. The models estimate the volume change for the 2016-2020 inter-eruptive inflation period to be between 0.054-0.060 km^3 and suggest that the MMR is compartmentalized, with most magma accumulating in sill-like bodies embedded in crystal mush along the western-central edge of the MMR. The results reveal the complexity of Axial's plumbing system and demonstrate the utility of integrating geodetic data and seismic imagery to gain deeper insights into magma storage at active volcanoes.

Plain Language Summary

Axial Seamount is a submarine volcano on the Juan de Fuca Ridge (NE Pacific Ocean) with enhanced magma supply from the Cobb Hotspot. Its frequent activity and long-term deformation time series covering eruptions in 1998, 2011 and 2015 make it an ideal place to study volcanic processes. Improved magma reservoir modeling at Axial will aid in understanding how magma transport and storage are related to surface deformation, seismicity, and eruption timing. Here we compare several models of Axial's magma reservoir to explore how the spatial component of the observed deformation at Axial compares to seismically imaged magma reservoir geometry. To constrain the models, we use vertical displacements covering an inflation period between 2016-2020, derived from pressure measurements collected at seafloor benchmarks and repeated bathymetric surveys. The models estimate the volume change for the 2016-2020 inflation period to be between 0.054-0.060 km^3. Our results suggest that the Axial's magma reservoir is compartmentalized, with most magma accumulating in sill-like bodies embedded in crystal mush. The results reveal the spatial complexity of Axial's plumbing system and demonstrate how deformation data and seismic imagery can be used together to gain deeper insights into magma storage at active volcanoes.

1. Introduction

Axial Seamount is an active submarine volcano located at the intersection of the Juan de Fuca Ridge and the Cobb hotspot about 500 km west of the Oregon coast in the NE Pacific (Figure 1). It has erupted at least 52 times over the last 800 years (Clague et al., 2013), most recently in 1998, 2011, and 2015. A nearly continuous deformation time series from 1998 through the present covering the past 3 eruptions has revealed that Axial exhibits a relatively repeatable inflation-deflation cycle, which has allowed for two successful eruption forecasts (Chadwick et al., 2012; Nooner & Chadwick, 2016). Even though Axial itself does not pose a direct threat to humans because of its remoteness, insight gleaned from observations made at Axial contribute to a growing body of knowledge about eruptive precursors that can be applied to more threatening locations.

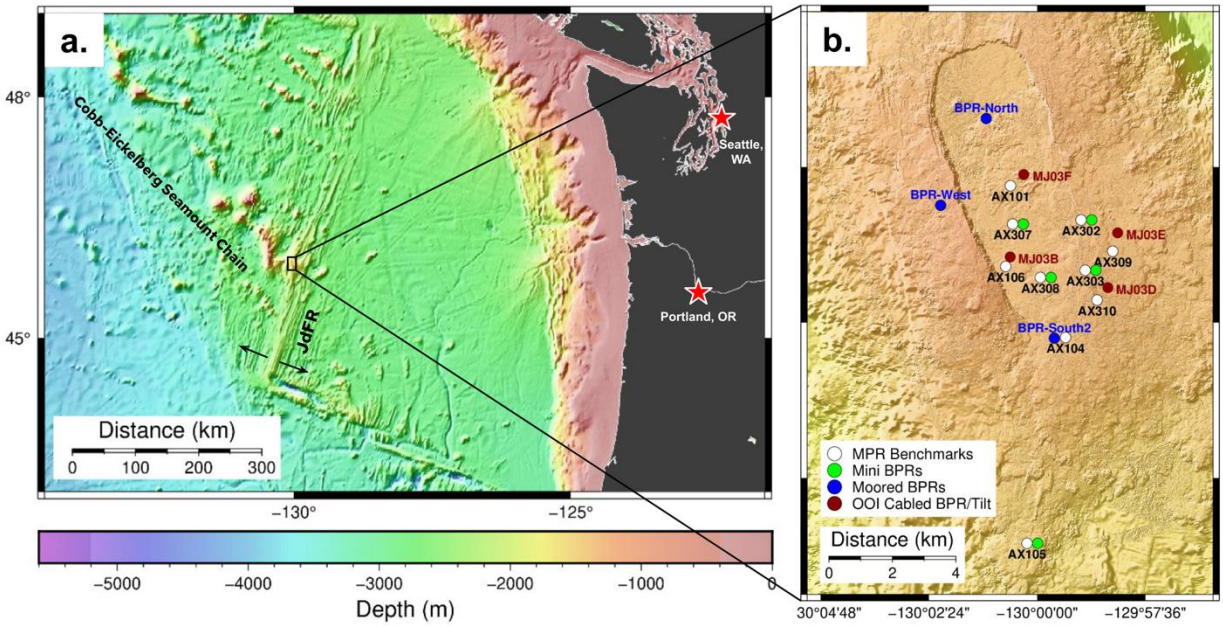

Figure 1. a) Axial Seamount's tectonic setting at the intersection of the Juan de Fuca Ridge (JdFR) and the Cobb hotspot. b) Zoom-in of Axial's summit caldera with geodetic instrumentation as of 2020 labeled. White dots are benchmarks where campaign-style mobile pressure recorder (MPR) measurements are made, green dots are mini bottom pressure recorders (BPRs), blue dots are moored BPRs, and red dots are BPRs and tilt meters connected to the Ocean Observatories Initiative (OOI) cabled observatory.

Deformation models of Axial have evolved from simple to more complex over the years as more geodetic data have become available. A point source (Mogi, 1958) was initially used as the pressure source when few observations were available to constrain models and little was known about the actual geometry of Axial's magma storage system (Chadwick et al., 2006; Nooner & Chadwick, 2009). Once more benchmarks for pressure measurements were added and more analytical model geometries were considered, a steeply dipping prolate spheroid geometry became the best-fit model (Hefner et al., 2020; Nooner & Chadwick, 2016). The prolate spheroid model depth, location, and geometry were somewhat consistent with a set of vertically stacked

deep sills later imaged by multi-channel seismic (MCS) data and interpreted by Carbotte et al., (2020). However, as autonomous underwater vehicle (AUV) repeat bathymetry data (Caress et al., 2020) has begun to provide more spatial coverage and therefore additional constraints for deformation modeling than the limited number of point-pressure observations alone, a rectangular horizontal sill deformation model with about the same outline as the summit caldera has been found to fit both the AUV and pressure data better than a prolate spheroid (Hefner et al., 2021).

The acquisition of multi-channel seismic (MCS) data at Axial (Arnulf et al., 2014, 2018; Carbotte et al., 2020) provided a high-resolution view of the magma reservoir geometry beneath the summit of Axial for the first time. Given the simplicity of the previous analytical deformation models, a logical next step was to investigate how a more realistic geometry of the magmatic system relates to deformation observed at the surface, in order to add more physical meaning to the modeling results. Arnulf et al., 2018 used MCS data to define the 3-D geometry and location of the main magma reservoir (MMR) beneath the summit caldera at Axial, as well as a secondary magma reservoir (SMR) to the east. The MMR vertically extends from 1.1-2.8 km depth below seafloor, is slightly offset from Axial's caldera to the east, and extends beyond the caldera to the north and south (Figure 2). The deep stacked sills imaged by Carbotte et al., (2020) are located below the southern half of the MMR between 3-5 km below the seafloor.

We constructed deformation models constrained by the MMR geometry in several ways. First, we directly used the 3D MMR geometry with uniform internal pressure in a finite element model (FEM), but we found that doing so provides very poor fit to the geodetic data. We then constructed and considered several analytical deformation models as alternatives, including: 1) approximating the MMR shape using one rectangular horizontal sill, 2) approximating the MMR shape using 3 rectangular non-horizontal sills, 3) allowing for non-uniform pressure distribution in a 2D horizontal sill at the average depth of the MMR roof, and 4) allowing for non-uniform pressure distributed over the 3D MMR roof. The models are constrained by the observations of vertical deformation from seafloor pressure data and repeated AUV bathymetric surveys during Axial's current inter-eruption phase between 2016-2020. Our inversion results suggest that the MMR is likely compartmentalized, which is consistent with current thinking on magma reservoir structure.

2. Deformation data

Bottom pressure recorders (BPRs) measure pressure at the seafloor; if the seafloor is uplifted, there is less water column above it and therefore lower pressure. Similarly, if the seafloor subsides, the BPR measures higher pressure. The pressure data are converted to depth after removing tidal signals (Eble et al., 1989). BPRs were deployed at Axial's summit caldera in 1998 when Axial's first observed eruption occurred (Chadwick et al., 2013; Dziak & Fox, 1999; Embley et al., 1999; Fox, 1999; Fox et al., 2001). After a two-year gap in coverage, the

deformation time series resumed in 2000 with an array of seafloor benchmarks and the time series has been continuous through the present (Figure 1; Chadwick et al., 2006, 2012, 2022; Nooner & Chadwick, 2009, 2016). Since 2000, BPR measurements have been supplemented by measurements from mobile pressure recorders (MPRs), which are used in campaign-style surveys at seafloor benchmarks with a remotely operated vehicle (ROV) every 1-2 years to correct for the BPRs' long-term drift where the two are co-located (Chadwick et al., 2006). We used the MPR data for our study instead of BPR data because there were more MPR measurement locations in 2016-2020 and we are more interested in the spatial component of deformation than the temporal component.

Bathymetric surveys at 1-m scale have been conducted at Axial since 2006 using multibeam sonar equipped AUVs, first to obtain comprehensive coverage of the volcanic terrain, and then to measure the extent and thickness of lava flows from the 2011 and 2015 eruptions through differencing of repeated surveys (Caress et al., 2012; Chadwick et al., 2016). Beginning after the most recent eruption in 2015, a new sparse pattern of AUV survey lines extending well outside the caldera (Figure 2) was established to measure vertical surface deformation by differencing (Caress et al., 2020); this pattern has been repeated each summer since except 2021. Differencing the repeated components of the surveys reveals vertical surface deformation over a broader area than from the pressure sensors alone. However, compared to the MPR data which has an accuracy of ±1 cm, the AUV repeat bathymetry data have a lower vertical displacement accuracy of ± 20 cm. We used AUV vertical displacement data between two surveys in 2016 and 2020 (Figure 2). An AUV bathymetric survey was also conducted in 2015, but this survey apparently had higher errors than subsequent surveys, because the AUV depth changes between 2015-2020 poorly match the MPR depth changes from the same time period. Since MPR measurements were made in 2015 and 2017 (but not in 2016), we estimated the uplift values in 2016 at the MPR benchmarks by interpolating between the 2015 and 2017 MPR measurements assuming a linear deformation rate. The BPR record shows that deformation at the center of the caldera during this time period was not entirely linear (Chadwick et al., 2022). The benchmark at the center of the caldera had uplifted by 55 cm from mid-2015 to mid-2016, about 10 cm shallower in summer of 2016 than a linear interpolation would predict (Figure S1 in Supplementary Material). The deformation rate is highest at this benchmark compared to the other benchmarks, so our interpolation introduces an additional uncertainty of ≤10 cm in the estimated 2016 benchmark depths. Nevertheless, the estimated 2016-2020 depth changes at the benchmarks agree relatively well with the 2016-2020 AUV data (Figure S2 in Supplementary Material).

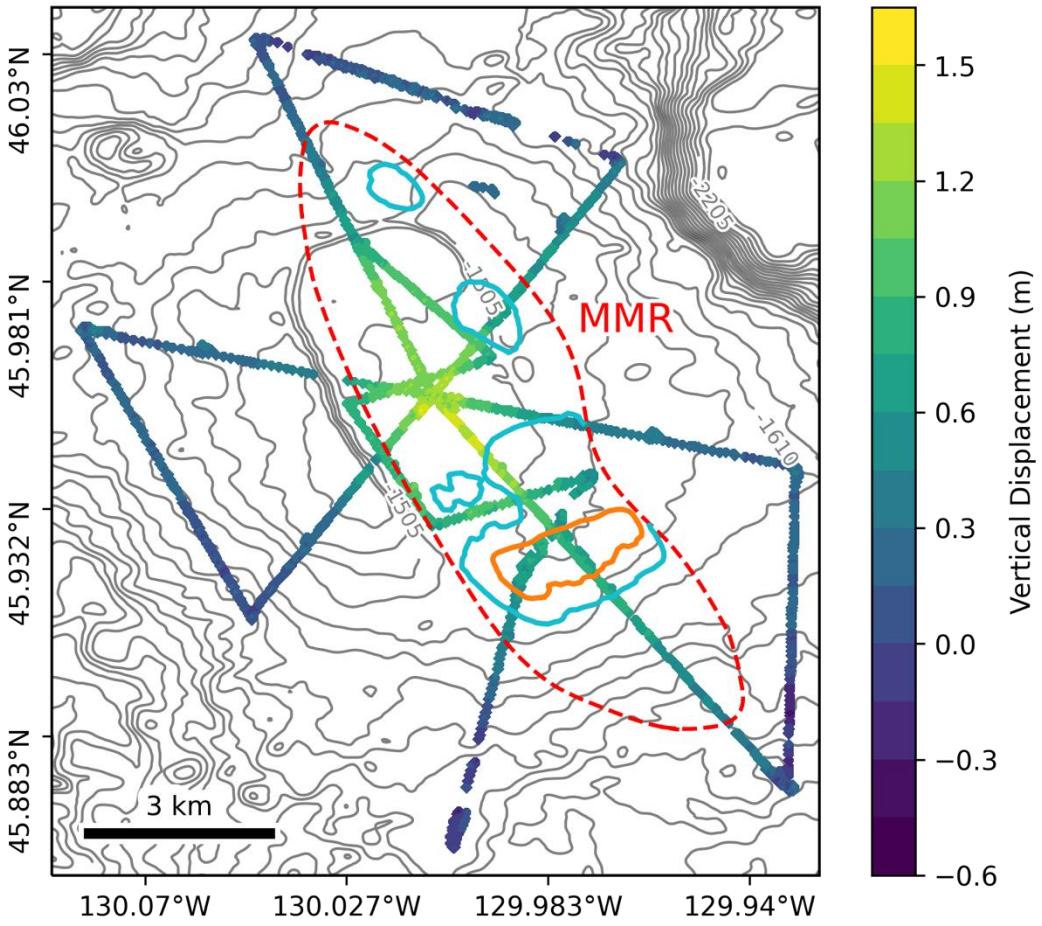

Figure 2. AUV repeat bathymetry data covering 2016-2020. Colors represent depth changes between AUV surveys. Background bathymetry contour interval is 35 m and select contours are labeled. The MMR is outlined with a red dotted line. The shallowest parts of the MMR roof are shown with depth contours at -1250m and -1500m (below seafloor) in orange and cyan, respectively.

We only used deformation data covering the inflation period from 2016 to 2020 to constrain our models because the main objective of our study is to investigate the spatial component of the deformation signal and its implications for the underlying magma storage system. Previous studies have shown that the spatial pattern of inflation does not vary significantly between different time periods (Nooner & Chadwick, 2016), except for major episodes of deflation during eruptions when slip on the caldera ring faults may contribute to the deformation field (Hefner et al., 2020).

3. Deformation modeling

Our objective was to improve upon previous deformation models by reconciling the MMR geometry with the observed spatial deformation pattern. To do this, we constructed a series of models with increasing complexity, all constrained/bounded by the MMR. Each is

discussed in detail below. For all models, typical mechanical properties were used (Poisson's ratio = 0.25, shear modulus = 30 GPa, Young's modulus = 70 GPa; Turcotte & Schubert, 2014). Table 1 contains a summary of model configurations, inversion methods, and performance. See Figures 3 and 4 for a comparison of model geometries.

	Model configuration	**Inversion method**	**Volume change (km^3)**	**$RMSE_{mpr}$ (m)**	**$RMSE_{auv}$ (m)**
Model 1	FEM, MMR with uniform internal pressure	Parameter search	0.173	0.312	0.254
Model 2a	Analytical, 1 rectangular, horizontal sill	MCMC	0.056	0.059	0.122
Model 2b	Analytical, 3 rectangular, non-horizontal sills	MCMC	0.06	0.047	0.097
Model 3a	Analytical, 2D horizontal grid of Okada sill sources	Least squares regression	0.06	0.009	0.130
Model 3b	Analytical, 3D Okada sill sources draped over MMR roof	Least squares regression	0.054	0.002	0.139

Table 1. Summary of model configurations, inversion methods, modeled volume changes, and Root Mean Square Error (RMSE) values between each model and the MPR and AUV data.

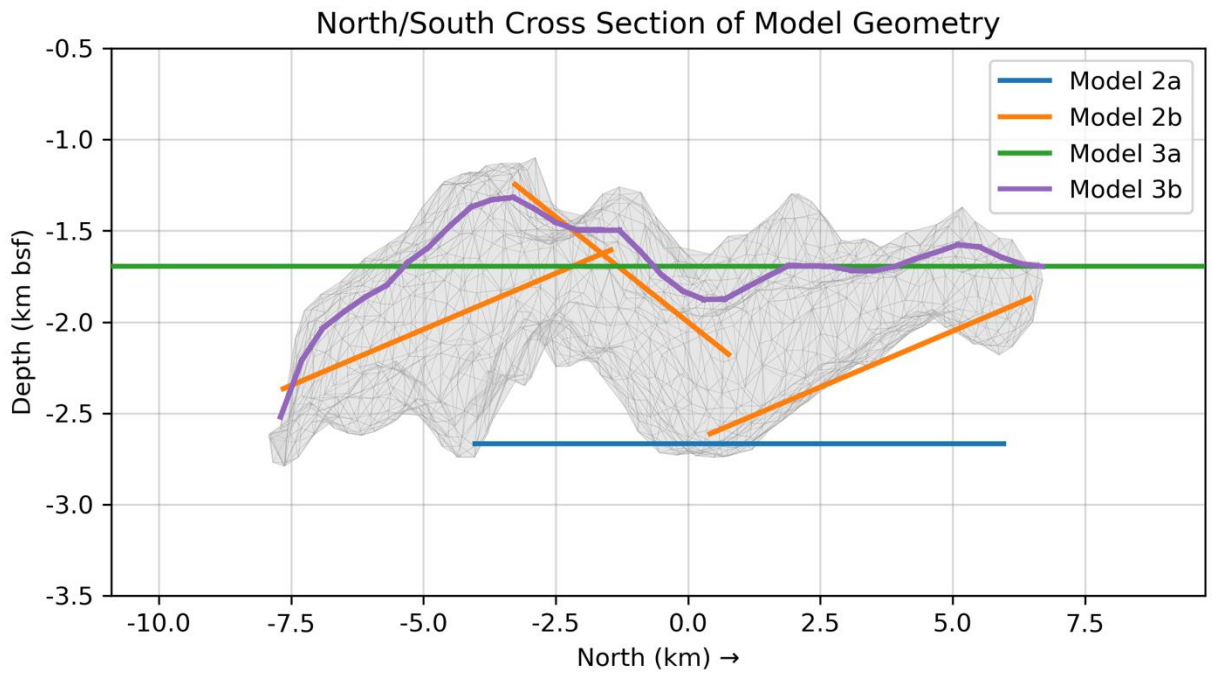

Figure 3. North/South cross section showing deformation model geometries investigated in this study. The MMR geometry from Arnulf et al., (2018) is shown as a gray mesh and represents the Model 1 FEM source geometry. The other models are single or multiple combination of rectangular Okada sills (colored lines) with either uniform or distributed (non-uniform) opening. See text for details.

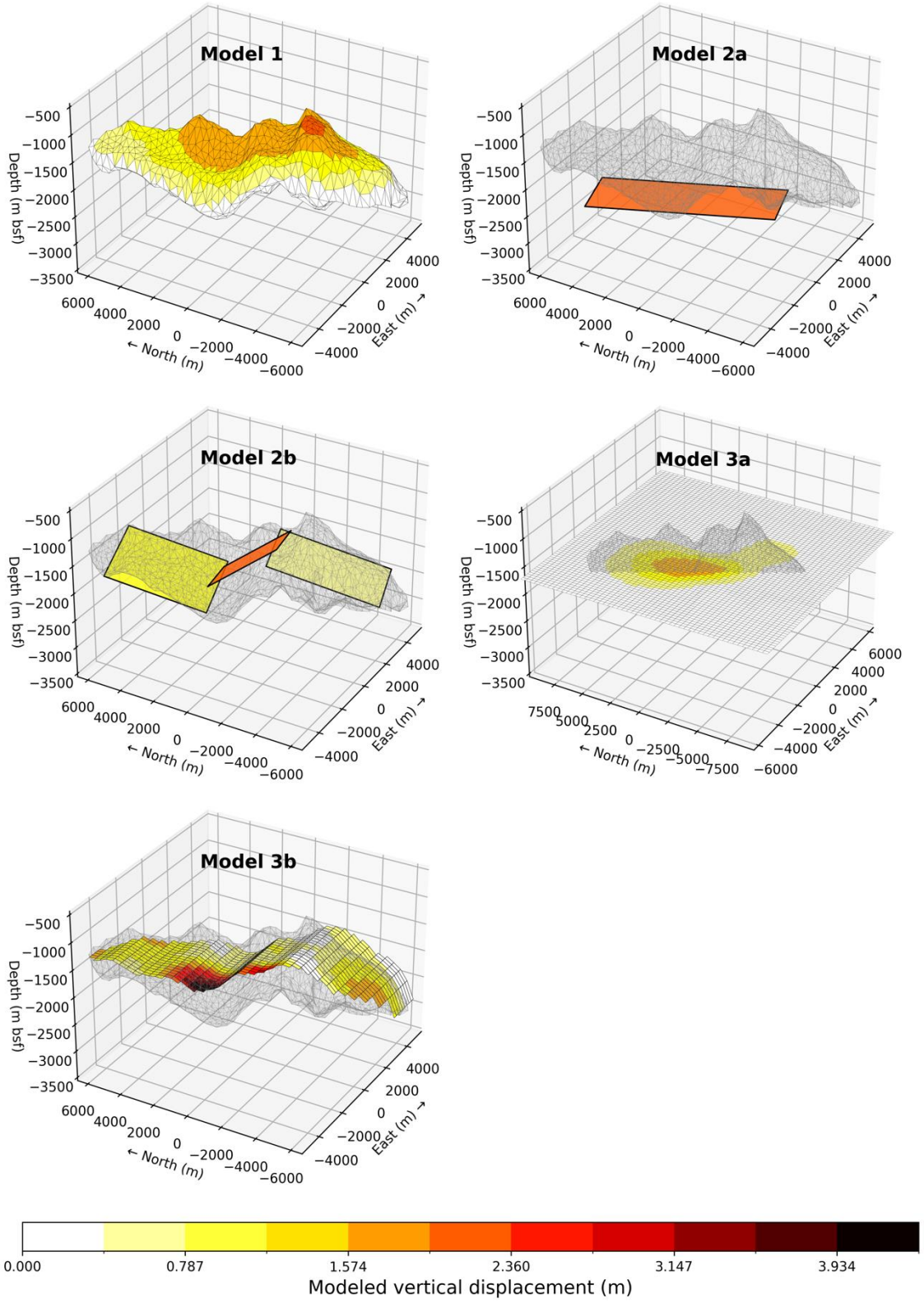

Figure 4. Model configurations and modeled openings of each pressure source. For Models 2a-3b, the MMR is shown as a transparent gray mesh to provide context for the model geometries.

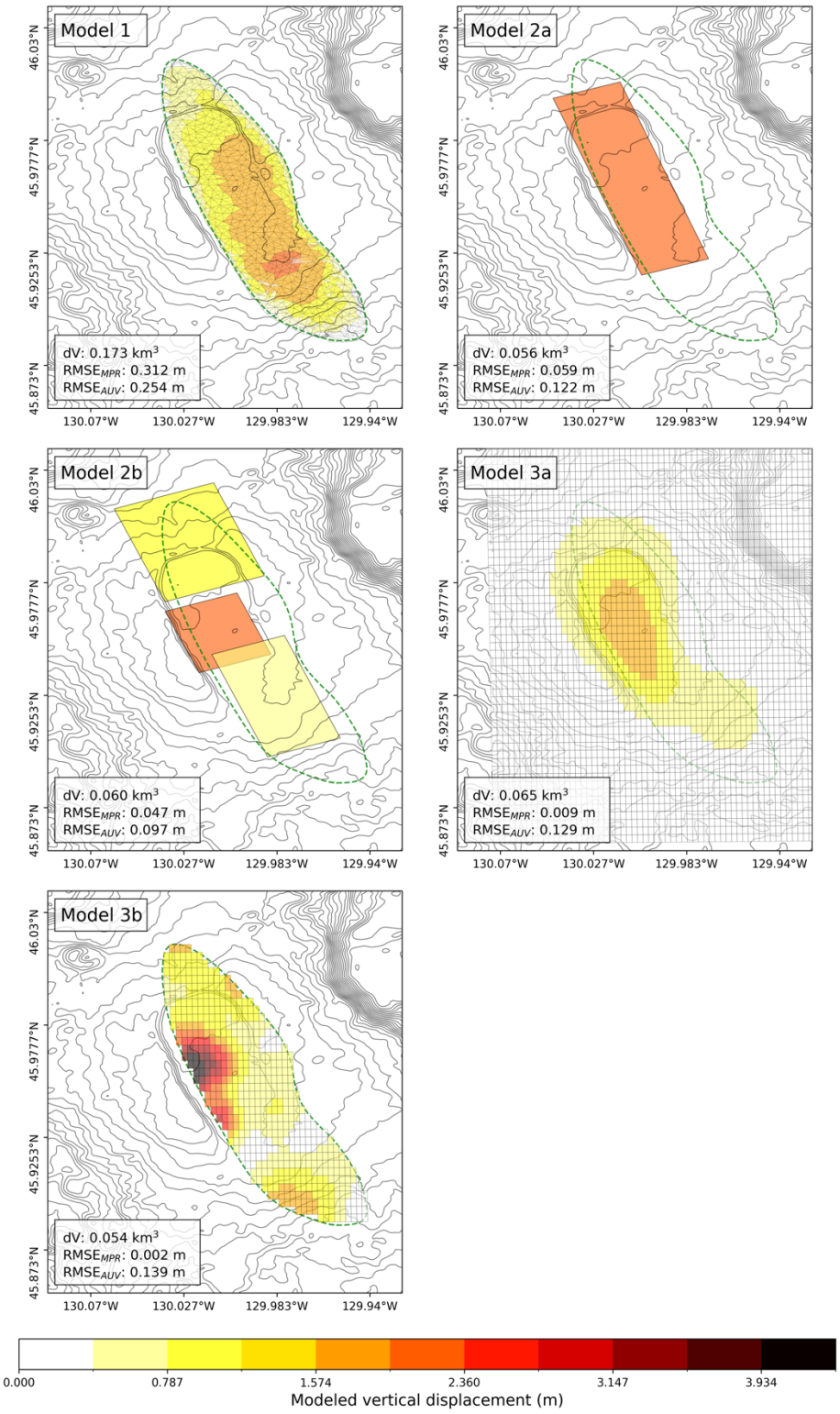

Figure 5. Model configurations and modeled openings of each pressure source overlain on bathymetric contours (each contour is 35 m). The MMR is outlined in each plot with a dotted green line. Each model's volume change (dV) and RMSE values between the model and the MPR and AUV data are plotted in the lower left corner of each panel.

Model 1a: Finite element model with MMR geometry and uniform pressure

As a first step, we constructed an FEM using the MMR geometry from Arnulf et al., 2018 with a uniform pressure source. We started with a 3D point cloud defining the combined MMR roof and floor (see Arnulf et al., 2018 for more detail on how the roof and floor boundaries were defined). A 3D surface was constructed from the point cloud using a ball-pivoting algorithm, which starts with a seed triangle and creates new triangles by pivoting a ball with user-defined radius around the edges until it meets new points (Bernardini et al., 1999). This 3D surface was then loaded into Abaqus/CAE 2020, which we used to carry out the FEM simulations. To validate the FEM methodology, we compared an analytical prolate spheroid model (Yang et al., 1988) to an FEM with a pressurized cavity of the same dimensions and verified that both models predict the same surface deformation (Figure S3 in Supplementary Material).

The FEM domain measures 50 km long x 50 km wide x 30 km deep and the boundary conditions were specified by a free top surface, a roller constraint on the side surfaces, and a fixed bottom surface. We added bathymetry to the model using GMRT bathymetry data (Ryan et al., 2009). The effect of gravity was accounted for by adding an additional analysis step (prior to pressurization of the source) in which gravitational equilibrium is established by adding a pre-stress defined by hydrostatic equilibrium. This is an 'initial guess' which is used as a starting point to solve for the gravitational force that balances out the pressure force to result in near-zero ground deformation according to a defined threshold. We tested the effect of ocean loading by adding a downward hydrostatic pressure applied to the seafloor and found it to be negligible.

The MMR was incorporated by subtracting its volume from the domain and applying a uniform internal pressure on the cavity walls. The pressure was varied over many simulations to minimize the combined root-mean-squared error (RMSE) between the modeled surface displacements and the AUV and MPR data.

3.1. Models 2a and 2b: Analytical sill models using Bayesian inference

Model 2a is a single rectangular horizontal sill (Okada, 1985) and Model 2b consists of 3 non-horizontal rectangular sills constrained by the MMR geometry. We used the Volcanic and Seismic Source Modeling (VSM) package (Trasatti, 2022) to conduct joint inversions using Markov chain Monte Carlo (MCMC) simulations to estimate the source parameters that produce surface deformation that best fits the AUV and MPR data.

For Model 2a, all inversion parameters were allowed to vary except for the dip angle of the sill, which was fixed at zero (horizontal). The sill's depth was bounded by the minimum and maximum MMR depth. For Model 2b, the 3-sill geometry was constrained by the MMR geometry by fixing the strike and dip angles in the inversion to follow the general trend of 3 main MMR segments (Figures 4 and 5). The locations of the sills were allowed to vary within 3

defined segments of the MMR volume and the sill opening values were allowed to vary freely. See Table 2 for a summary of fixed and best-fit variable parameters for Models 2a and 2b.

		Centroid Longitude	Centroid Latitude	Centroid depth (m bsf)	Length (m)	Width (m)	Strike	Dip	Opening (m)
Model 2a		-130.0100 ± 258 m	45.9637 ± 110 m	2666 ± 306	2561 ± 1119	9680 ± 253	341° ± 2	0	2.256 ± 0.682
Model 2b	**Sill 1**	-130.0249 ± 79 m	45.9968 ± 77 m	2241 ± 74	3829 ± 170	5170 ± 115	340°	-7°	1.285 ± 0.041
	Sill 2	-130.0110 ± 83 m	45.9543 ± 97 m	1712 ± 70	2769 ± 166	3475 ± 164	340°	13°	2.071 ± 0.152
	Sill 3	-129.9850 ± 126 m	45.9265 ± 175 m	1985 ± 206	2800 ± 207	5707.36 ± 325	340°	-7°	0.893 ± 0.076

Table 2. Summary of fixed and best-fit inverted parameters with standard deviations for Models 2a and 2b. The strike angle is the orientation of the plane measured clockwise from North according to Okada (1985) (i.e., strike = 0 if the plane is oriented North-South and dips to the East, strike = 90 if the plane is oriented East-West and dips to the South). Fixed parameters have red shading, parameters allowed to vary within the confines of the MMR geometry have yellow shading, and parameters allowed to freely vary have green shading.

3.2. Models 3a and 3b: 2D and 3D distributed pressure inversions

Inverting geodetic data to determine variable slip or opening distribution is a standard method for inferring co-seismic slip on faults (e.g., Moreno et al., 2009) and has also been applied in volcanic settings (e.g., Grandin et al., 2009). We performed two joint inversions of the MPR and AUV data following this approach. For Model 3a, we created a 2D horizontal grid of rectangular sill-patches at the average depth of the MMR roof and extending beyond the MMR boundary horizontally by 3 km in both the x and y directions. For Model 3b, we gridded the MMR roof point cloud into rectangular patches where each patch is defined by its position, length, width, strike, and dip. The patches are allowed to dip to the North/South but not East/West to create a continuous 3D grid with no gaps; this is appropriate since there is much more dip variation along the North/South direction of the MMR than there is along the East/West direction. The depths of the patches were defined by the average MMR roof depth at that location (Figures 3 and 4).

For both Models 3a and 3b, we treated each patch as a rectangular dislocation (Okada, 1985) and inverted for the opening value of each patch. Posed as a forward problem, the relationship between surface displacements and patch openings can be expressed by the linear system:

$$d = Gm$$

where d is the observation vector composed of vertical surface displacements, G is the Green's function matrix, and m is the vector of model parameters (patch openings). G was constructed by computing the expected vertical displacement at every observation point for each patch caused by a unit opening on that patch. To solve for m, we used a regularized linear least squares method which minimizes the objective function, $\phi(m)$:

$$\phi(m) = \| W(G \cdot m - d) \|_2^2 + \lambda^2 \| L \cdot m \|_2^2$$

The first term $\| W(G \cdot m - d) \|_2^2$ represents weighted misfit, i.e., the squared Euclidean norm difference between the observed data and the data predicted by the model, where W is a diagonal weight matrix which normalizes the contribution of the MPR and AUV datasets based on the relative uncertainties and the number of relative data points. The second term $\lambda^2 \| L \cdot m \|_2^2$ is the regularization term, where λ is the regularization parameter that controls the smoothness of the model, and L is the regularization matrix. The optimal λ value was chosen using an L-curve, where the preferred smoothness is located at the corner of the curve created by plotting roughness vs. the L2 norm of misfit (Figure 6).

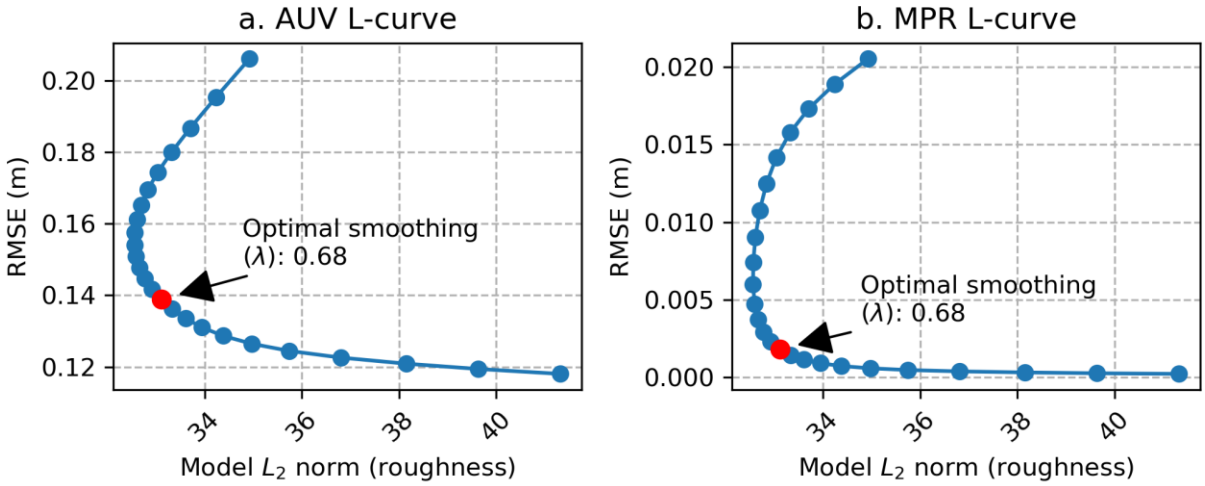

Figure 6. L-curves showing model roughness vs. Root Mean Square Error (RMSE) as a measure of misfit between the model and the data for (a) the AUV data and (b) the MPR data. The optimal smoothness occurs at the corner of the curve. Example shown is for Model 3b.

3.3. Weighing the AUV and MPR data

We weighed the AUV and MPR data on a case-by-case basis for each model due to differences among inversion methods. For Model 1, since the best-fit model was found by a parameter search over uniform pressure values on the MMR surface (all other model parameters were fixed), we calculated the AUV RMSE and MPR RMSE for each iteration then normalized them by dividing each by the maximum RMSE value across all iterations and by the relative uncertainties in the datasets. We then calculated the combined RMSE for each iteration by summing the normalized AUV RMSE and MPR RMSE values. The optimal model was chosen

as the model with the lowest combined RMSE value. For Models 2a and 2b, we first weighed the datasets in an MCMC simulation according to their relative uncertainties, then further adjusted the weights over many MCMC simulations to find the weight combination that minimized the combined AUV and MPR RMSE values.

For Models 3a and 3b, we found a tradeoff between the regularization parameter λ and the relative weights, due to higher noise in the AUV data than in the MPR data. Instead of just normalizing the AUV and MPR datasets using their relative uncertainties, we further normalized them by the number of data points in each dataset. The λ value was then chosen as described above in Section 3.3.

4. Results

We found that Model 1 (uniform pressurization of the 3-dimensional MMR) did not fit either the MPR or AUV data well. This was not unexpected, since the MMR geometry is offset from the caldera to the east while the observed deformation is centered on the caldera. Also, the shallowest features along the MMR roof are located beneath the SE part of the caldera and because of this, the model creates the largest surface deformation there, 4-5 km SE of the caldera center (Figures 2, 4a and 6a). This makes sense intuitively since these shallowest MMR features have less overburden and therefore uplift more readily under uniform pressurization. This result tells us that the observed deformation cannot be simply produced by uniform pressure within the entire MMR, which suggests that perhaps the MMR is compartmentalized with isolated melt pockets that are not well connected. The other four models, which were developed to test this idea, showed increasing improvement of fit to the MPR data as more parameters were added, and the AUV RMSE values were also improved, but not as much and varied from model to model (Table 1). We suspect that this is because of the higher uncertainty associated with the AUV data, which was factored into how the datasets were weighed.

Despite differences among model geometries, the models consistently estimated a best-fit volume change of between 0.054-0.060 km^3, except for Model 1 which estimated 0.173 km^3. Modeled deformation and fit to the MPR data are plotted in Figure 7 and AUV repeat bathymetry residuals are plotted in Figure 8. In Models 3a and 3b where pressure was allowed to spatially vary, modeled pressure changes were highest along the western-central edge of the MMR (Figures 4 and 5). There is also a region of positive pressure change in the southern-most southward dipping region of the MMR due to a long wavelength deformation signal present in this area in the AUV data.

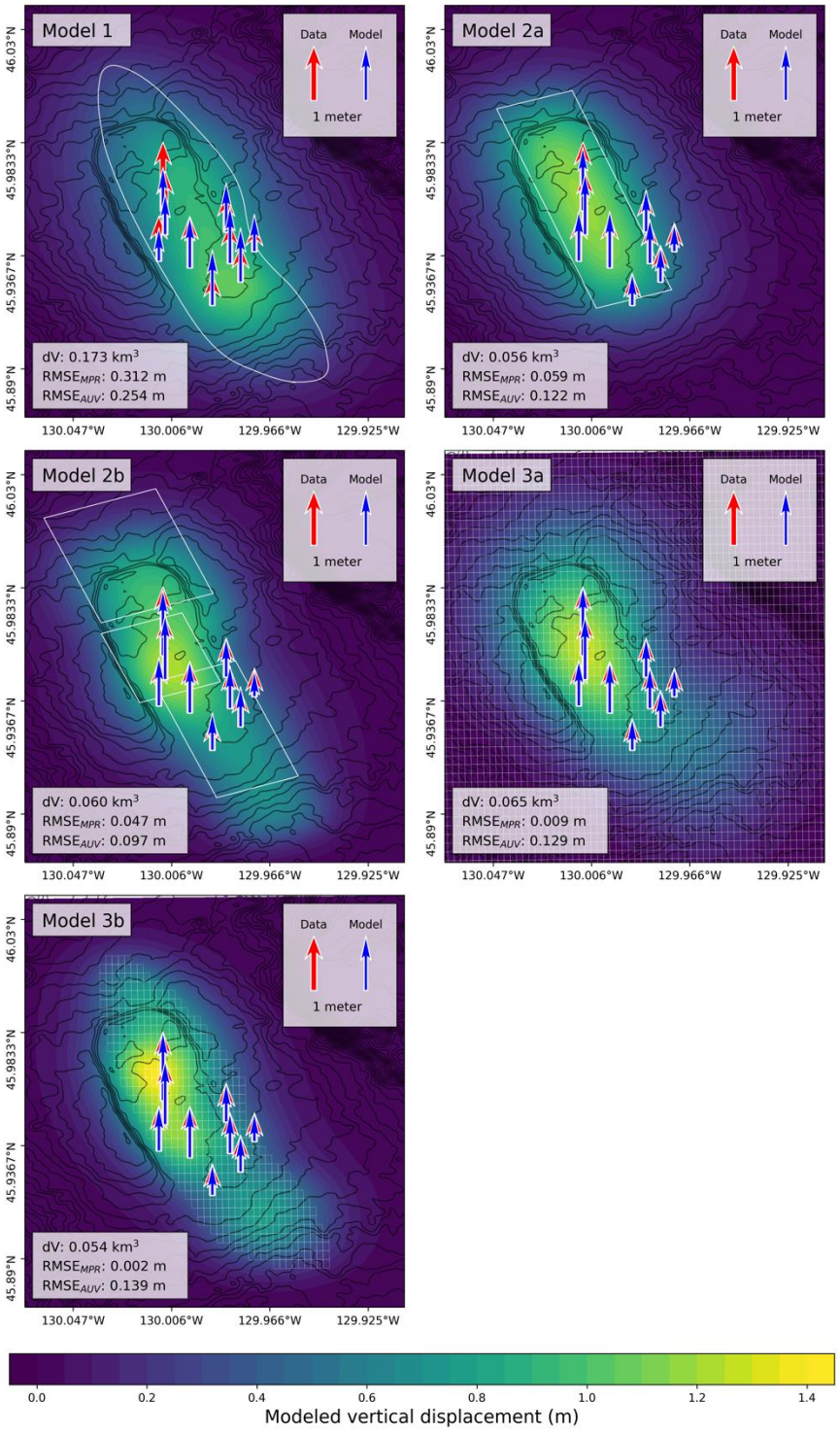

Figure 7. Predicted surface vertical deformation for all best-fit models with comparison between the MPR data (red arrows) and modeled surface displacements (blue arrows). The surface projection of each model geometry is shown as a white outline. Each model's volume change (dV) and rmse values between the model and the MPR and AUV data are plotted in the lower left corner of each panel.

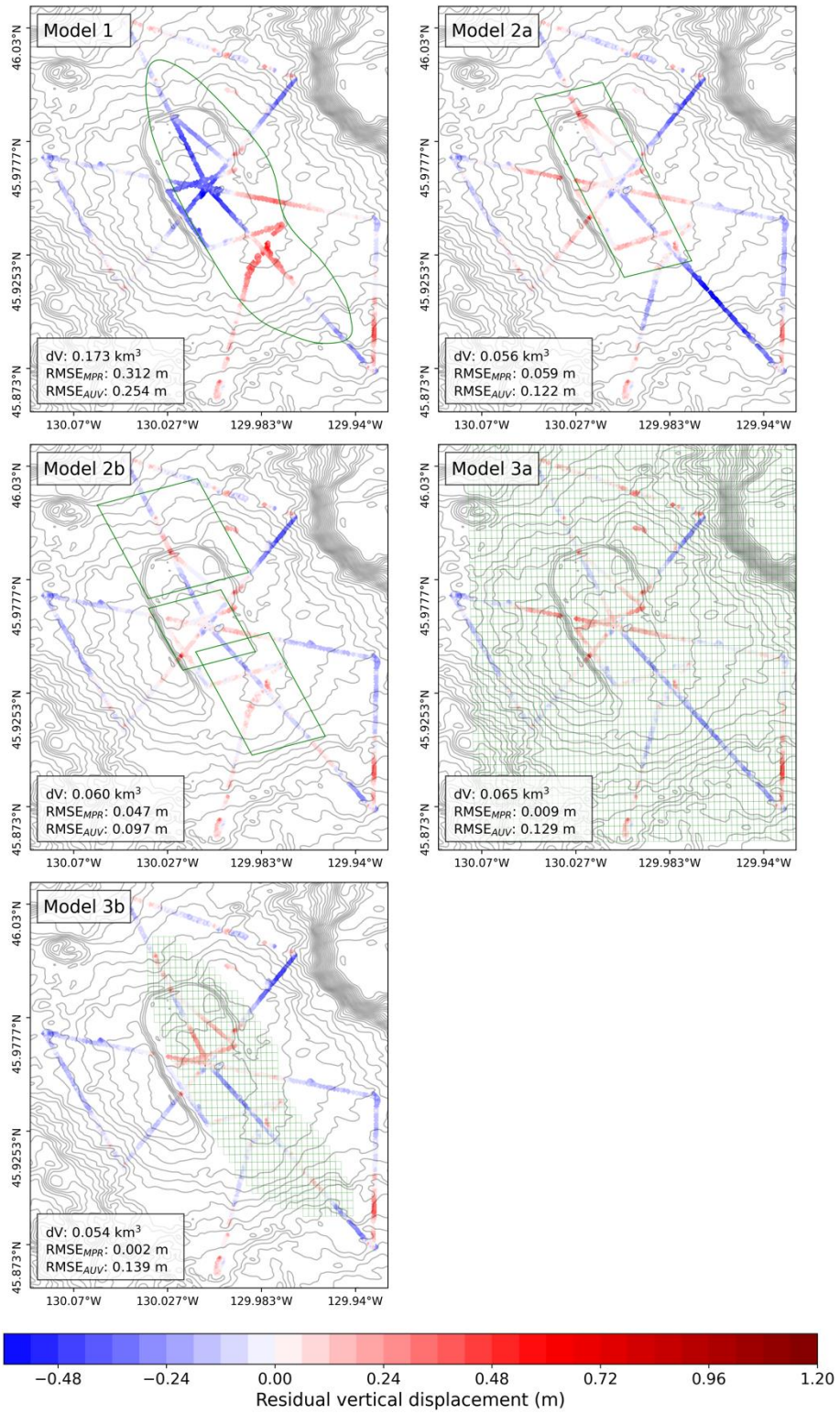

Figure 8. AUV repeat bathymetry residuals plotted by subtracting the modeled displacements from the AUV data. The surface projection of each model geometry is plotted as a green outline. Each model's volume change (dV) and rmse values between the model and the MPR and AUV data are plotted in the lower left corner of each panel.

5. Discussion

5.1. Model assumptions and limitations

All our models assume homogeneous and isotropic elastic half spaces (except for Model 1, which includes bathymetry). Masterlark (2007) showed that the presence of layered crustal material can increase source depth estimates when compared to models assuming elastic half spaces with uniform properties. Since Axial's volcanic edifice is composed of lava flows emplaced upon one another over time, there is likely some anisotropy in which stiffness is different in the vertical and lateral directions, which could cause an underestimation of source depths. In addition, we found in sensitivity testing that inclusion of Axial's bathymetry in a finite element model using a prolate spheroid pressure source fixed at a depth of 3.8 km (the best-fit model of Nooner & Chadwick, 2016) can affect the volume change estimate by up to 27% (Figure S3 in Supplementary Material). This effect would increase with shallower source depths (Williams & Wadge, 1998) such as at the depth of the MMR. This result was unexpected because of Axial's relatively modest bathymetric relief, so more work must be done to better understand which bathymetric features (e.g., caldera walls vs surrounding bathymetric features) influence the expression of vertical deformation for a given pressure source geometry.

Our assumption of elasticity could also affect the modeling results since there may be non-elastic or viscoelastic effects unaccounted for in the models. Numerical modeling implementing viscoelasticity at Mt. Etna has shown that lower pressures can produce the same deformation as elastic models with higher pressure due to viscoelastic relaxation over time (Del Negro et al., 2009). Depending on where this region of viscoelasticity is defined (either above or below the pressure source), this phenomenon could result in either inflation or deflation observed on the surface (Nooner & Chadwick, 2009). Cabaniss et al., (2020) found that non-temperature-dependent elastic rheology requires greater reservoir overpressures to reproduce the observed surface deformation at Axial compared to models that incorporate a temperature-dependent rheology. Additionally, petrological and tomographic studies increasingly show that magma reservoirs are likely composed of discrete melt lenses/sills embedded within a crystal-rich magma mush (Cashman et al., 2017). Magma mush is expected to behave poroelastically/poroviscoelastically (Gudmundsson, 2012; Liao et al., 2018, 2021). Although viscoelastic effects and the presence of magma mush would likely not significantly impact the spatial distribution of modeled pressure changes in our results, it could impact volume change estimates due to magma compressibility. Modeling viscoelastic effects at Axial would be more strongly relevant to the temporal component of the deformation time series, for example to test hypotheses regarding short-term deflation events proposed by Chadwick et al., (2022).

We also assumed that Axial's spatial deformation pattern does not vary temporally, except for during eruptions when there may be slip on the caldera ring faults (Hefner et al., 2020; Levy et al., 2018). The degree to which these ring faults are activated during Axial's inter-eruptive periods is unknown. Although there is little evidence of slip on these faults during the

2016-2020 inflation in the AUV repeat bathymetry data (in the form of a sharp offsets along AUV track lines crossing the faults), the uncertainty in the AUV data (± 20 cm) may be equal to or higher than the amount of expected slip (8-30 cm; Levy et al., 2018). An FEM that includes bathymetry, spatially variable pressure, and inclusion of ring faults would be most thorough, although the number of free parameters in a complex model like this may not be constrainable by the current deformation data. Recent expansions of the geodetic monitoring network at Axial will be able to better quantify any slip across the caldera faults in the future.

5.2. Implications for magma storage beneath Axial caldera

A best-fitting deformation model cannot reveal the exact geometry of a magma storage system and should not be interpreted as such; rather, a deformation model can provide the approximate location and volume changes of the region(s) where the greatest pressure changes occurred during inter-eruption magma supply into the storage system. While our results provide improved horizontal constraints on where magma accumulates between eruptions, there is inherent non-uniqueness among modeled depths due to the tradeoff between depth and pressure. While our best-fit horizontal sill (Model 2a) is similar in horizontal geometry to the best-fit horizontal sill found by Hefner et al. (2021), the depth of our sill is deeper at 2.7 km compared to 0.97-1.24 km, which is likely due to differences in inversion methods and/or the tradeoff between depth and pressure.

Despite this tradeoff, the consistent volume change estimates of 0.054-0.060 km^3 among Models 2a-3b suggests that the volume change is not significantly sensitive to model depths within the depth range of the MMR. In addition, we tested an FEM model using the prolate spheroid geometry (best-fit solution from Nooner & Chadwick, 2016) constrained only by the 2015-2020 MPR data, which resulted in a volume change of 0.077 km^3 (Figure S3a in Supplementary Material). Since this included an extra year's worth of inflation compared to the 2016-2020 models we show in this study, the estimated volume change for the 2016-2020 time period would be somewhat lower, more or less consistent with the volume change estimates using geometries constrained by the MMR above. This demonstrates that the estimated volume change for this inter-eruptive recharge period is not highly sensitive to model geometry, depth, or location.

The total volume of the shallow magma storage system beneath Axial was estimated by Arnulf et al. (2014) to be 18-30 km^3 and the modeled co-eruptive volume change associated with previous eruptions has been estimated to vary between 0.147 – 0.206 km^3 using analytical model source depths of 3-3.8 km (Chadwick et al., 1999, 2012; Hefner et al., 2020; Nooner & Chadwick, 2016). Our study models the observed inflation from 2016-2020, during a time when the magma supply rate was initially high, but then waned with time following the 2015 eruption (Chadwick et al., 2022). Given that the magma supply rate is estimated to have varied from >0.1

km^3/year to <0.01 km^3/year during that time period (Chadwick et al., 2022), our volume change estimates are reasonable.

Mullet & Segall (2022) demonstrated that as the melt fraction of mush in a magma reservoir increases, the deformation caused by a mush-dominated magma storage system is increasingly driven by the overall shape of the mush body, instead of any pressurized melt lens within the mush. If the melt fraction within the MMR is high enough to cause Axial's deformation to be driven by the entire mushy body (instead of individual sills) and if we assume that the MMR is a continuous body, it follows that using the MMR geometry as a pressure source should fit the deformation data. The poor fit to the data of Model 1 as well as the pattern of pressure distribution in Models 3a and 3b are instead suggestive of compartmentalization of melt within the MMR and a relatively low melt fraction in the surrounding mush (Figure 9). In this context, compartmentalization means that melt bodies within the MMR are not connected hydraulically, at least on time scales that are relevant to the deformation cycle at Axial.

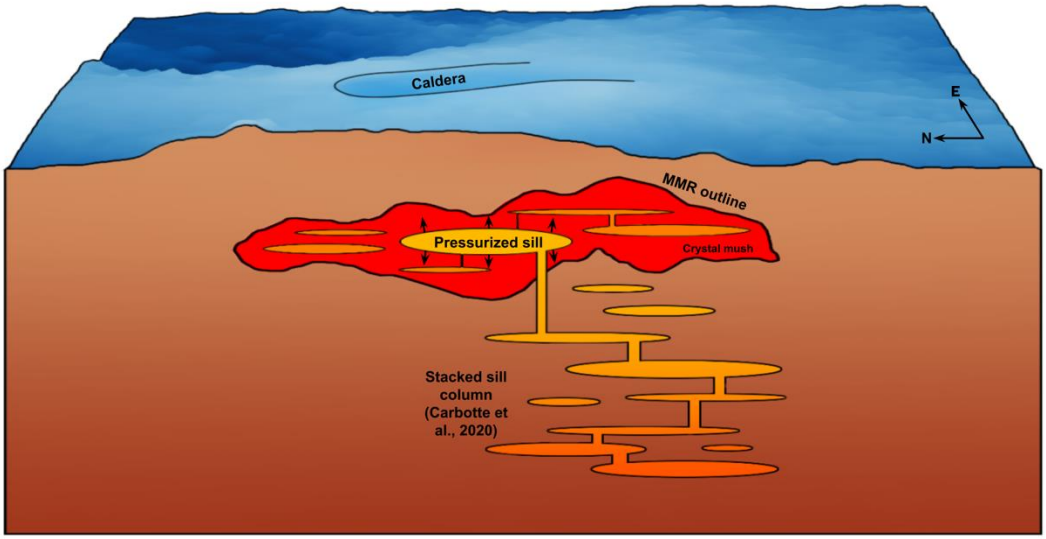

Figure 9. Schematic diagram illustrating possible compartmentalized melt distribution in which sills are emplaced in crystal mush both within and below the MMR.

The depth of magma residence estimated by petrological analyses (Dreyer et al., 2013) is deeper at 3-6 km than the MMR depth range of 1.1-2.8 km, but is consistent with the deeper system of stacked sills beneath the MMR imaged by Carbotte et al., 2020 extending from 3-5 km depth below seafloor. Since we did not consider deformation sources in this depth range, we cannot rule out contribution to the deformation field of a potential pressure source (or multiple sources) in the stacked sill region. Non-uniqueness among models due to the tradeoff between depth/pressure would likely hinder efforts to resolve pressurization of multiple vertically stacked sills or the combination of compartmentalized MMR pressurization with a source representing the stacked sill region. However, since the stacked sills are exclusively beneath the SSE part of

the caldera, they probably cannot produce the observed caldera-centered deformation by themselves.

6. Conclusions

The ability to accurately forecast volcanic eruptions is an important goal in hazard mitigation research. Linking precursory signals like ground deformation to subsurface processes is therefore essential. With the increase in spatial coverage of Axial's deformation monitoring due to the application of AUV repeat bathymetric surveys, there is now adequate data to justify more complex deformation modeling than what has been done previously. We constructed a suite of numerical and analytical models geometrically constrained by the shape of the seismically imaged MMR to investigate the role of the MMR in creating the observed surface deformation and to test the hypothesis that the MMR is compartmentalized. Although our estimated volume change of 0.054-0.060 km^3 for the inflation period between 2016-2020 is reasonable considering previous estimates of inflation and eruption volumes, the models make assumptions (flat seafloor, full elasticity, no ring faults) that could influence the volume change and/or depth estimates. Nevertheless, the models with spatially varying pressure (Models 3a and 3b) suggest that magma accumulates during Axial's inter-eruptive recharge periods along the western-central edge of the MMR with some potential additional accumulation in the southern-most southward dipping region of the MMR. Future modeling efforts with additional complexity and more parameters will likely require increased data constraints in the form of higher resolution seismic imagery and/or horizontal deformation measurements.

Acknowledgements

Collection of data used in this study was funded by the National Science Foundation (awards OCE-1736926, 1736882, and 1737019) and the David and Lucille Packard Foundation. The authors are grateful to Adrien Arnulf for providing the MMR top and bottom horizon geometry. The authors also thank the crews of R/V Thompson, R/V Kilo Moana, R/V Zephyr, and R/V Rachel Carson for their support at sea, the ROV Jason team (WHOI National Deep Submergence Facility) for conducting the MPR surveys, and the operational teams of AUV Sentry (WHOI National Deep Submergence Facility) and the MBARI Mapping AUVs for conducting the AUV surveys.

Data Availability Statement

The code and data used for this research can be found at https://zenodo.org/records/10219997. Academic licensing for Abaqus software is provided by Simulia, Dassault Systèmes. The VSM software used for analytical modeling can be found at https://github.com/EliTras/VSM (Trasatti, 2022).

References

Arnulf, A. F., Harding, A. J., Kent, G. M., Carbotte, S. M., Canales, J. P., & Nedimović, M. R. (2014). Anatomy of an active submarine volcano. *Geology*, *42*(8), 655–658. https://doi.org/10.1130/G35629.1

Arnulf, A. F., Harding, A. J., Kent, G. M., & Wilcock, W. S. D. (2018). Structure, Seismicity, and Accretionary Processes at the Hot Spot-Influenced Axial Seamount on the Juan de Fuca Ridge. *Journal of Geophysical Research: Solid Earth*, *123*(6), 4618–4646. https://doi.org/10.1029/2017JB015131

Bernardini, F., Mittleman, J., Rushmeier, H., Silva, C., & Taubin, G. (1999). The ball-pivoting algorithm for surface reconstruction. *IEEE Transactions on Visualization and Computer Graphics*, *5*(4), 349–359. https://doi.org/10.1109/2945.817351

Cabaniss, H. E., Gregg, P. M., Nooner, S. L., & Chadwick, W. W. (2020). Triggering of eruptions at Axial Seamount, Juan de Fuca Ridge. *Scientific Reports*, *10*(1), 1–11. https://doi.org/10.1038/s41598-020-67043-0

Carbotte, S. M., Arnulf, A., Spiegelman, M., Lee, M., Harding, A., Kent, G., Canales, J. P., & Nedimović, M. (2020). Stacked sills forming a deep melt-mush feeder conduit beneath axial seamount. *Geology*, *48*(7), 693–697. https://doi.org/10.1130/G47223.1

Caress, D. W., Clague, D. A., Paduan, J. B., Chadwick, W. W., Nooner, S. L., & Thomas, H. J. (2020). Vertical Deformation of the Axial Seamount Summit from Repeated 1-m Scale Bathymetry Surveys Using AUVs. In *American Geophysical Union, Fall Meeting 2020, abstract #V040-0017*.

Caress, D. W., Clague, D. A., Paduan, J. B., Martin, J. F., Dreyer, B. M., Chadwick, W. W., Denny, A., & Kelley, D. S. (2012). Repeat bathymetric surveys at 1-metre resolution of lava flows erupted at Axial Seamount in April 2011. *Nature Geoscience*, *5*(7), 483–488. https://doi.org/10.1038/ngeo1496

Cashman, K. V., Sparks, R. S. J., & Blundy, J. D. (2017). Vertically extensive and unstable magmatic systems: A unified view of igneous processes. *Science*, *355*(6331). https://doi.org/10.1126/science.aag3055

Chadwick, W. W., Clague, D. A., Embley, R. W., Perfit, M. R., Butterfield, D. A., Caress, D. W., Paduan, J. B., Martin, J. F., Sasnett, P., Merle, S. G., & Bobbitt, A. M. (2013). The 1998 eruption of Axial Seamount: New insights on submarine lava flow emplacement from high-resolution mapping. *Geochemistry, Geophysics, Geosystems*, *14*(10), 3939–3968. https://doi.org/10.1002/ggge.20202

Chadwick, W. W., Embley, R. W., Milburn, H. B., Meinig, C., & Stapp, M. (1999). Evidence for deformation associated with the 1998 eruption of Axial Volcano, Juan de Fuca Ridge, from acoustic extensometer measurements. *Geophysical Research Letters*, *26*(23), 3441–3444. https://doi.org/10.1029/1999GL900498

Chadwick, W. W., Nooner, S. L., Butterfield, D. A., & Lilley, M. D. (2012). Seafloor deformation and forecasts of the April 2011 eruption at Axial Seamount. *Nature Geoscience*, *5*(7), 474–477. https://doi.org/10.1038/ngeo1464

Chadwick, W. W., Nooner, S. L., Zumberge, M. A., Embley, R. W., & Fox, C. G. (2006). Vertical deformation monitoring at Axial Seamount since its 1998 eruption using deep-sea pressure sensors. *Journal of Volcanology and Geothermal Research*, *150*(1–3), 313–327. https://doi.org/10.1016/j.jvolgeores.2005.07.006

Chadwick, W. W., Paduan, J. B., Clague, D. A., Dreyer, B. M., Merle, S. G., Bobbitt, A. M., Caress, D. W., Philip, B. T., Kelley, D. S., & Nooner, S. L. (2016). Voluminous eruption from a zoned magma body after an increase in supply rate at Axial Seamount. *Geophysical Research Letters*, *43*(23), 12,063-12,070. https://doi.org/10.1002/2016GL071327

Chadwick, W. W., Wilcock, W. S. D., Nooner, S. L., Beeson, J. W., Sawyer, A. M., & Lau, T. K. (2022). Geodetic Monitoring at Axial Seamount Since Its 2015 Eruption Reveals a Waning Magma Supply and Tightly Linked Rates of Deformation and Seismicity. *Geochemistry, Geophysics, Geosystems*, *23*(1). https://doi.org/10.1029/2021GC010153

Clague, D. A., Dreyer, B. M., Paduan, J. B., Martin, J. F., Chadwick, W. W., Caress, D. W., Portner, R. A., Guilderson, T. P., McGann, M. L., Thomas, H., Butterfield, D. A., & Embley, R. W. (2013). Geologic history of the summit of Axial Seamount, Juan de Fuca Ridge. *Geochemistry, Geophysics, Geosystems*, *14*(10), 4403–4443. https://doi.org/10.1002/ggge.20240

Del Negro, C., Currenti, G., & Scandura, D. (2009). Temperature-dependent viscoelastic modeling of ground deformation: Application to Etna volcano during the 1993-1997 inflation period. *Physics of the Earth and Planetary Interiors*, *172*, 299–309. https://doi.org/10.1016/j.pepi.2008.10.019

Dreyer, B. M., Clague, D. A., & Gill, J. B. (2013). Petrological variability of recent magmatism at Axial Seamount summit, Juan de Fuca Ridge. *Geochemistry, Geophysics, Geosystems*, *14*(10), 4306–4333. https://doi.org/10.1002/ggge.20239

Dziak, R. P., & Fox, C. G. (1999). The January 1998 Earthquake swarm at Axial Volcano, Juan de Fuca Ridge: Hydroacoustic evidence of seafloor volcanic activity. *Geophysical Research Letters*, *26*(23), 3429–3432. https://doi.org/10.1029/1999GL002332

Eble, M. C., Gonzalez, F. I., Mattens, D. M., Milburn, H. B., Mosbacher, R. A., Knauss, J. A., & Fletcher, J. O. (1989). *Instrumentation, field operations, and data processing for PMEL deep ocean bottom pressure measurements*.

Embley, R. W., Chadwick, W. W., Clague, D., & Stakes, D. (1999). 1998 eruption of axial volcano: Multibeam anomalies and sea-floor observations. *Geophysical Research Letters*, *26*(23), 3425–3428. https://doi.org/10.1029/1999GL002328

Fox, C. G. (1999). In situ ground deformation measurements from the summit of Axial Volcano during the 1998 volcanic episode. *Geophysical Research Letters*, *26*(23), 3437–3440. https://doi.org/10.1029/1999GL900491

Fox, C. G., Chadwick, W. W., & Embley, R. W. (2001). Direct observation of a submarine volcanic eruption from a sea-floor instrument caught in a lava flow. *Nature 2001 412:6848*, *412*(6848), 727–729. https://doi.org/10.1038/35089066

Grandin, R., Socquet, A., Binet, R., Klinger, Y., Jacques, E., De Chabalier, J. B., King, G. C. P., Lasserre, C., Tait, S., Tapponnier, P., Delorme, A., & Pinzuti, P. (2009). September 2005 Manda hararo-dabbahu rifting event, Afar (Ethiopia): Constraints provided by geodetic data. *Journal of Geophysical Research: Solid Earth*, *114*(8). https://doi.org/10.1029/2008JB005843

Gudmundsson, A. (2012). Magma chambers: Formation, local stresses, excess pressures, and compartments. *Journal of Volcanology and Geothermal Research*, *237–238*, 19–41. https://doi.org/10.1016/j.jvolgeores.2012.05.015

Hefner, W. L., Nooner, S. L., Chadwick, W. W., & Bohnenstiehl, D. R. (2020). Revised Magmatic Source Models for the 2015 Eruption at Axial Seamount Including Estimates of Fault-Induced Deformation. *Journal of Geophysical Research: Solid Earth*, *125*(4), e2020JB019356. https://doi.org/10.1029/2020JB019356

Hefner, W., Nooner, S. L., Chadwick, W. W., Caress, D. W., Paduan, J. B., Bohnenstiehl, D. R., & Clague, D. A. (2021). Deformation Models for the 2015-Eruption and Post-Eruption Inflation at Axial Seamount from Repeat AUV Bathymetry. In *AGU Fall Meeting 2021, held in New Orleans, LA, 13-17 December 2021, id. V45B-0138.*

Levy, S., Bohnenstiehl, D. R., Sprinkle, P., Boettcher, M. S., Wilcock, W. S. D., Tolstoy, M., & Waldhauser, F. (2018). Mechanics of fault reactivation before, during, and after the 2015 eruption of Axial Seamount. *Geology*, *46*(5), 447–450. https://doi.org/10.1130/G39978.1

Liao, Y., Soule, S. A., & Jones, M. (2018). On the Mechanical Effects of Poroelastic Crystal Mush in Classical Magma Chamber Models. *Journal of Geophysical Research: Solid Earth*, *123*(11), 9376–9406. https://doi.org/10.1029/2018JB015985

Liao, Y., Soule, S. A., Jones, M., & Le Mével, H. (2021). The Roles of Heat and Gas in a Mushy Magma Chamber. *Journal of Geophysical Research: Solid Earth*, *126*(4). https://doi.org/10.1029/2020JB019395

Masterlark, T. (2007). Magma intrusion and deformation predictions: Sensitivities to the Mogi assumptions. *Journal of Geophysical Research*, *112*(B6), B06419. https://doi.org/10.1029/2006JB004860

Mogi, K. (1958). Relations between the eruptions of various volcanoes and the deformations of the ground surfaces around them. *Bull. Earthq. Res. Inst.*, *36*, 99–134. https://ci.nii.ac.jp/naid/10017329458/

Moreno, M. S., Bolte, J., Klotz, J., & Melnick, D. (2009). Impact of megathrust geometry on inversion of coseismic slip from geodetic data: Application to the 1960 Chile earthquake. *Geophysical Research Letters*, *36*(16). https://doi.org/10.1029/2009GL039276

Mullet, B., & Segall, P. (2022). The Surface Deformation Signature of a Transcrustal, Crystal Mush-Dominant Magma System. *Journal of Geophysical Research: Solid Earth*, *127*(5). https://doi.org/10.1029/2022JB024178

Nooner, S. L., & Chadwick, W. W. (2009). Volcanic inflation measured in the caldera of axial seamount: Implications for magma supply and future eruptions. *Geochemistry, Geophysics, Geosystems*, *10*(2). https://doi.org/10.1029/2008GC002315

Nooner, S. L., & Chadwick, W. W. (2016). Inflation-predictable behavior and co-eruption deformation at Axial Seamount. *Science*, *354*(6318), 1399–1403. https://doi.org/10.1126/SCIENCE.AAH4666

Okada, Y. (1985). Surface deformation due to shear and tensile faults in a half-space. *Bulletin of the Seismological Society of America*, *75*(4), 1135–1154.

Ryan, W. B. F., Carbotte, S. M., Coplan, J. O., O'Hara, S., Melkonian, A., Arko, R., Weissel, R. A., Ferrini, V., Goodwillie, A., Nitsche, F., Bonczkowski, J., & Zemsky, R. (2009). Global multi-resolution topography synthesis. *Geochemistry, Geophysics, Geosystems*, *10*(3). https://doi.org/10.1029/2008GC002332

Trasatti, E. (2022). Volcanic and Seismic Source Modeling: An Open Tool for Geodetic Data Modeling. *Frontiers in Earth Science*, *10*. https://doi.org/10.3389/feart.2022.917222

Turcotte, D. L., & Schubert, G. (2014). *Geodynamics* (3rd ed.). Cambridge University Press.

Williams, C., & Wadge, G. (1998). The effects of topography on magma chamber deformation models: Application to Mt. Etna and radar interferometry. *Advances in Difference Equations*, *25*(10), 1549–1552. https://doi.org/10.1186/s13662-019-2194-1

Yang, X. M., Davis, P. M., & Dieterich, J. H. (1988). Deformation from inflation of a dipping finite prolate spheroid in an elastic half-space as a model for volcanic stressing. *Journal of Geophysical Research*, *93*(B5), 4249–4257. https://doi.org/10.1029/JB093iB05p04249